H/V Analysis in Juchitán de Zaragoza, Oaxaca, Following the 2017 **M** 8.2 Tehuantepec, México, Earthquake

Solymar Ayala Cortez[*1], Aaron A. Velasco[1], Marianne S. Karplus[1], Oscar S. Dena Ornelas[1,2], Hector Gonzalez-Huizar[1,3], Xyoli Pérez-Campos[4], Allen Husker[4,5], and Mohan Pant[1]

ABSTRACT

In September 2017, over 450 lives were lost in Mexico as a result of two unusual, large-magnitude, normal earthquakes. On 7 September, an *M* 8.2 earthquake occurred offshore of the State of Oaxaca in the Gulf of Tehuantepec, one of the largest extensional earthquakes to have occurred in a subduction zone. Twelve days later on 19 September an *M* 7.1 damaging earthquake struck near Puebla and Morelos, over 600 km away. Both earthquakes occurred in the downgoing Cocos plate, which is subducting beneath the North American plate. The first large event was followed on 23 September by a shallow *M* 6.1 extensional earthquake near Juchitán de Zaragoza, Oaxaca. Researchers from Mexico and the United States collaborated to deploy a temporary seismic network to study the aftershocks of the *M* 8.2 Tehuantepec, Mexico, earthquake, which included a three-week deployment of 51 Magseis Fairfield Z-Land 5-Hz three-component nodal seismometers ("nodes") near Juchitán and a 6-month deployment of 10 Nanometrics Trillium 120PA broadband seismometers with Reftek RT130 dataloggers for 6 months. In this article, we analyze the capabilities of the nodes to calculate the horizontal/vertical (H/V) spectral ratio and relative amplification using both microtremors and earthquakes and validate the results calculated with the nodes using data from broadband stations from this and previous deployments in the area. We create maps showing a correlation of the distribution of the fundamental frequency and relative amplification of the soil and compare them with the geology and the damage caused by the September 2017 earthquakes. There is a lack of public awareness and discrepancies in the construction procedures in the region, and we find that the majority of damaged houses in the area of study followed the location of river beds and tended to be in places with low resonance frequencies despite being in a low amplification zone.

KEY POINTS

- We test a nodal array and analyze site effects in areas damaged by the 2017 Tehuantepec earthquake.
- Nodes can derive H/V curves effectively similar to broadbands but with the advantage of portability.
- Nodes can be used to create high-quality maps of site effects to help the reconstruction of vulnerable areas.

Supplemental Material

INTRODUCTION

The 7 September 2017 *M* 8.2 Tehuantepec earthquake, one of the largest extensional earthquakes to have occurred in the subduction zone, initiated offshore at a depth of ~57 km. The rupture propagated up-dip to the northwest along a high-angle normal fault (strike: 315° and dip: 81°) within the downgoing Cocos slab along the Middle America trench (MAT). The earthquake had a seismic moment of 1.74×10^{21} N · m (M_w 8.2; Melgar, Ruiz-Angulo, *et al.*, 2018; Suárez *et al.*, 2019; Zhang and Brudzinski, 2019). The 19 September 2017 *M* 7.1 earthquake near Morelos–Puebla occurred over 600 km to the

1. Department of Geological Sciences, University of Texas at El Paso, El Paso, Texas, U.S.A., https://orcid.org/0000-0001-9227-1016 (SAC); https://orcid.org/0000-0003-0695-6153 (AAV); https://orcid.org/0000-0001-6007-5790 (MSK); https://orcid.org/0000-0002-3514-5424 (OSDO); https://orcid.org/0000-0001-8937-732X (HG-H); 2. Departmento de Física, Universidad Autónoma de Ciudad Juárez, Chih, Mexico; 3. Centro de Investigación Científica y de Educación Superior de Ensenada, Baja California, Ensenada, Mexico; 4. Instituto de Geofísica, Universidad Nacional Autónoma de México, Ciudad de México, Mexico, https://orcid.org/0000-0001-8970-7966 (XP-C); https://orcid.org/0000-0003-1139-0502 (AH); 5. Seismological Laboratory, California Institute of Technology, Pasadena, California, U.S.A.

*Corresponding author: sayalacortez@miners.utep.edu

Cite this article as Cortez, S. A., A. A. Velasco, M. S. Karplus, O. S. Dena Ornelas, H. Gonzalez-Huizar, X. Pérez-Campos, A. Husker, and M. Pant (2022). H/V Analysis in Juchitán de Zaragoza, Oaxaca, Following the 2017 **M** 8.2 Tehuantepec, México, Earthquake, *Bull. Seismol. Soc. Am.* **113**, 804–822, doi: 10.1785/0120210141

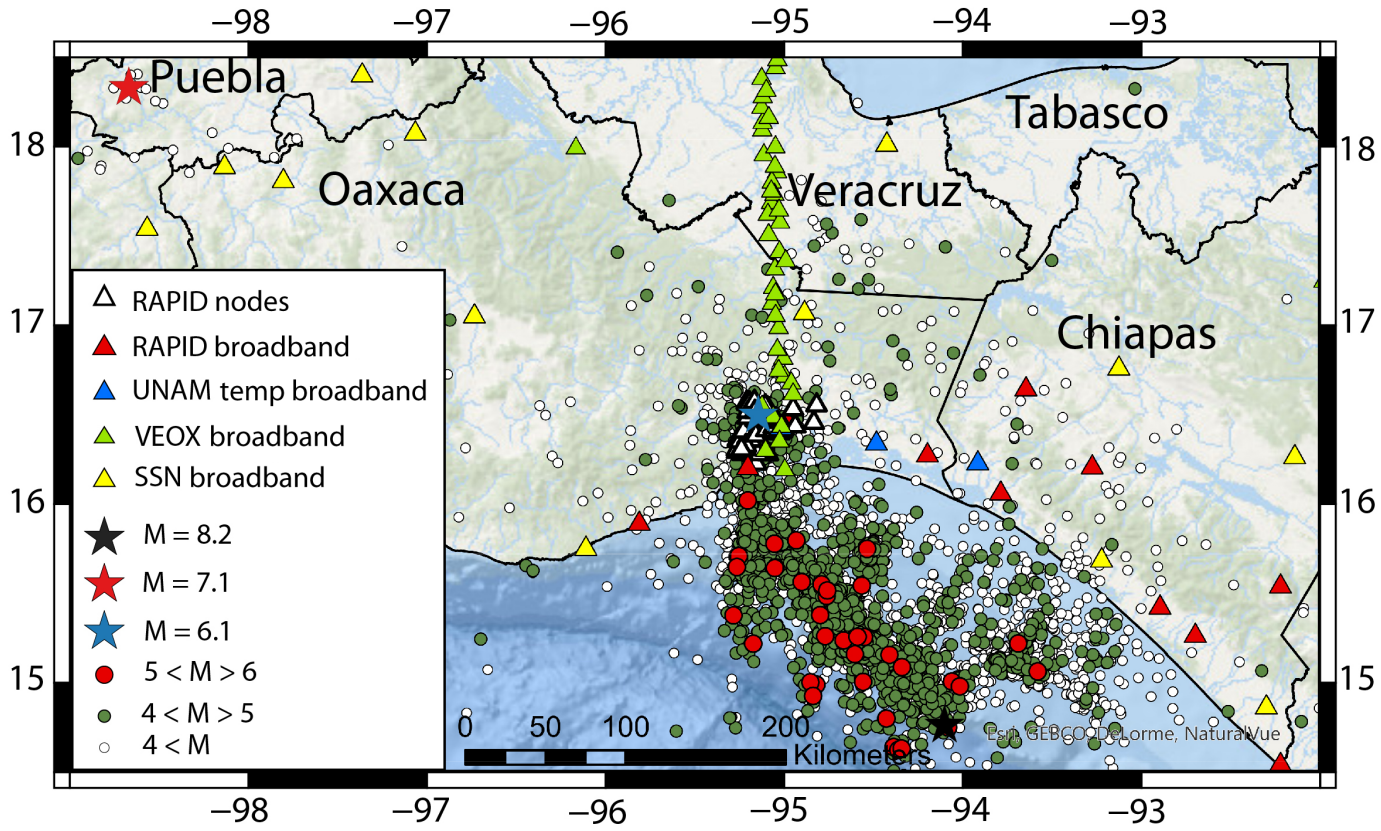

Figure 1. Map of south Mexico showing seismic activity before the nodal deployment recorded by Servicio Sismológico Nacional (SSN) from 1–30 September 2017 that includes the **M** 8.2 Tehuantepec earthquake (black star), the **M** 7.1 Morelos Puebla earthquake (red star), and the **M** 6.1 aftershock under Juchitán de Zaragoza (blue star). The seismic cluster that sparked our interest to deploy the rapid-response seismic network (RAPID) nodal deployment (white triangles) in Juchitán is shown with green, red, and white circles. The blue triangles show the location of the temporary stations deployed by Universidad Nacional Autónoma de México (UNAM) to record aftershocks of the Tehuantepec earthquake, and the yellow triangles show the permanent Servicio Sismológico Nacional (SSN) network in the area. The red triangles show the location of the broadband stations, and the orange triangles represent the location of the permanent stations deployed by SSN. Overlaying the distribution of permanent and temporal stations deployed to record aftershocks of the Tehuantepec earthquake and the location of a previous network (VEOX) deployed during 2008–2009 to study Tehuantepec tectonics. The color version of this figure is available only in the electronic edition.

northwest and exhibited an extensional focal mechanism within the downgoing Cocos plate, initiating at a depth of ~57 km with a dip angle of 44°–47° (Melgar, Pérez-Campos, *et al.*, 2018). Figure 1 shows the locations of these events and their aftershocks determined by the Servicio Sismológico Nacional (SSN) during September 2017. The Tehuantepec and Morelos–Puebla earthquakes considerably impacted the areas near their epicenters, causing an estimated loss of 369 lives in Mexico City and 99 lives in Oaxaca, Chiapas, Veracruz, and Tabasco, plus a total economic loss of $4.277 billion U.S. (Centro Nacional de Prevención de Desastres [CENAPRED], 2018).

Along this convergent boundary, thrust focal mechanism events dominate the region, which is expected for a subduction zone. These two normal faulting events underscore the importance of hazard mitigation in Mexico and highlight the need to understand atypical extensional earthquakes along the MAT (e.g., Pardo and Suárez, 1995). The largest aftershock of the Tehuantepec earthquake occurred on 23 September 2017 near Ixtepec and was a shallow (~10 km depth) **M** 6.1 extensional earthquake that occurred onshore in Oaxaca, creating more damage and aftershocks in the region (Melgar, Ruiz-Angulo, *et al.*, 2018). The importance of studying this region was reemphasized with the occurrence of the 23 June 2020 **M** 7.4 La Crucecita earthquake (Velasco *et al.*, 2020), a shallow thrust event that occurred on the subduction interface just north of the Tehuantepec aftershocks that created significant damage in the region.

Following the seismic events that occurred in September 2017, researchers from Universidad Nacional Autónoma de México (UNAM), Universidad Autónoma de Ciudad Juarez in Mexico, and the University of Texas at El Paso (UTEP) teamed to deploy a rapid-response seismic network (RAPID), funded by the National Science Foundation (NSF). Figure 1 also shows the distribution of the network and highlights our study area. The rapid-response network focused on recording the copious aftershocks following the *M* 8.2 Tehuantepec, México, earthquake by augmenting the permanent and temporary

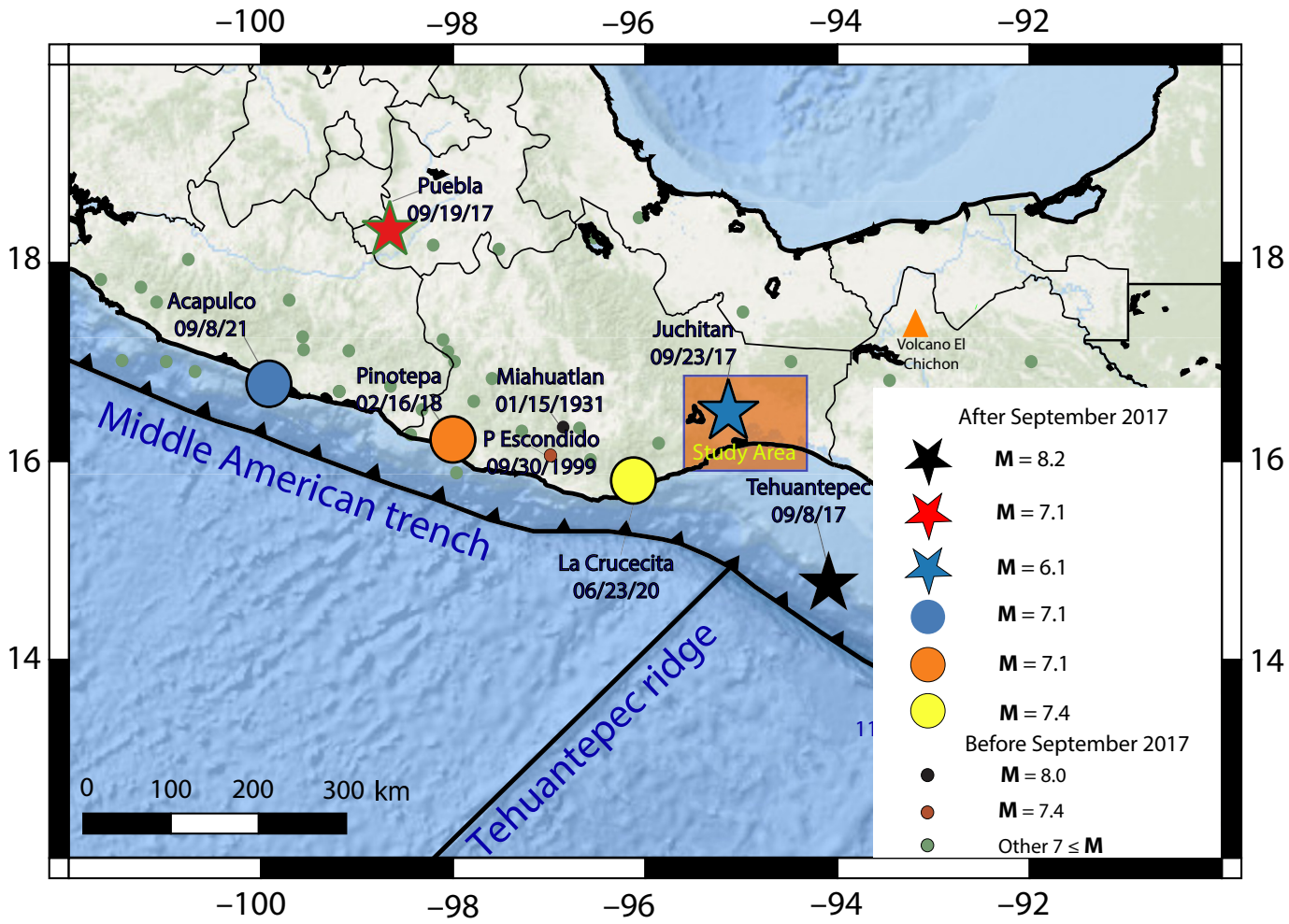

networks deployed by UNAM. Specifically, in early October 2017, 10 broadband seismometers were deployed for six months, and 51 seismic nodes (5 Hz, three-component geophones) were deployed for 22 days (due to limited battery life). Our node network overlapped some of the previously broadband station deployments.

We focus on analyzing the node data to quantify site effects and compare to the observed significant and varied damage in Juchitán de Zaragoza and the surrounding region (CENAPRED *et al.*, 2017). We test the capabilities of the nodal network to quantify the H/V peak frequency in the Juchitán region using noise and earthquake data. Specifically, we used the microtremor horizontal-to-vertical spectral ratio (MHVSR) technique using microtremor noise data to obtain the natural frequency of the soils and used earthquake data to define site amplification and generate contour maps showing the geographical distribution of these parameters. We then compare our results to the damage distribution in the region from the September 2017 earthquakes.

TECTONIC SETTING AND SEISMICITY

Our area of study surrounds Juchitán de Zaragoza, Oaxaca, which is located in southern Mexico near the Gulf of Tehuantepec. Oaxaca, one of the most seismically active states in Mexico, is affected by the offshore subduction of the Cocos plate beneath the North American plate along the MAT (Fig. 2). Near the location where the Tehuantepec ridge is subducted, the dip of the subducting slab changes from shallow (in the north) to steep (in the south) (Pérez-Campos *et al.*, 2008; Dougherty and Clayton, 2014). Large thrust events on adjacent megathrust segments as well as normal-faulting events, such as the 1931 *M* 8.0 Oaxaca earthquake and the 2017 Tehuantepec earthquake, have impacted Juchitán (Fig. S1, available in the supplemental material to this article). Normal-faulting earthquakes within oceanic subducting slabs have been explained by

Figure 2. Distribution of all earthquakes larger than *M* 7 recorded by SSN around the study area before and after September 2017. The blue star also shows the location of the main aftershock of the Tehuantepec earthquake that contribute to the damage of Juchitán de Zaragoza. The Middle American trench and the Tehuantepec ridge are significant ocean floor features. A younger ocean floor is being subducted north of the Tehuantepec ridge, (map obtained by UNAVCO model GSRM v. 2.1 from Kreemer *et al.*, 2014). The color version of this figure is available only in the electronic edition.

slab bending, slab pull forces, and complex interactions of fluids and changing heat regimes (Lynnes and Lay, 1988; Beck and Christensen, 1991; Ammon *et al.*, 2008; Lay *et al.*, 2013; Singh *et al.*, 2014; Melgar, Ruiz-Angulo, *et al.*, 2018). Some suggest outer rise fault reactivation allowed the entire subducting lithospheric slab to rupture as a result of the 2017 Tehuantepec extensional earthquake (e.g., Ye *et al.*, 2017; Melgar, Ruiz-Angulo, *et al.*, 2018; Suárez *et al.*, 2019; Zhang and Brudzinski, 2019).

Major seismic events prior to 2017

The subduction zone near the 2017 Tehuantepec earthquake can be considered a mature seismic gap, a region that has not had a large event in the past 100 yr. The last great subduction interface earthquake near this region occurred in 1902 (Suárez *et al.*, 2019) and appeared to have ruptured above the southern part of the 2017 rupture. However, recent relocations and intensity analysis suggest this event was intraplate (Suárez, 2020; Suárez *et al.*, 2020). Prior to the 1902 earthquake, in 1787 an **M** ∼8.6 earthquake is believed to have ruptured the plate interface to the northern segment of the Gulf of Tehuantepec, Oaxaca, and the southern Guerrero Coast (Suárez and Albini, 2009). Two previous intraplate normal earthquakes, one on 30 September 1999 *M* 7.4 and the other on 15 January 1931 *M* 7.8, ruptured just beneath the seismogenic plate boundary to the north of the 2017 Tehuantepec epicenter (Singh *et al.*, 1985, 2000). The 1999 normal earthquake had a depth of 39 km (SSN) and an approximate fault area of 80 by 30 km (Singh *et al.*, 2000; Bravo *et al.*, 2004). The 1931 normal earthquake occurred near the epicenter of the 1999 earthquake at a depth of ∼40 km (Singh *et al.*, 1985).

Foreshocks, aftershocks, and afterslip

The foreshocks, aftershocks, and afterslip of the Tehuantepec earthquake show a complex pattern (Fig. S1). Meng *et al.* (2019) use template matching to show that a foreshock sequence occurred one day before the Tehuantepec earthquake within 30 km of the hypocenter. They also show that a calibrated *P*-wave backprojection approach has significant energy release northward of the Tehuantepec ridge. Guo *et al.* (2019) show that the cumulative afterslip during the six months after the mainshock occurred north of the original mainshock, with a seismic moment of 1.58×10^{11} N · m (M_w 8.0).

The SSN recorded over 30,000 aftershocks from the Tehuantepec sequence during six months following the earthquake (Servicio Sismológico Nacional [SSN], 2018), highlighting the significant amount of seismicity that this earthquake generated. Suárez *et al.* (2019) relocated 301 events using careful analysis of *P* and *S* waves for aftershocks prior to 23 September 2017. They show the complexity of the rupture, in which the majority of the events lie outside the mainshock fault that ruptured. The aftershocks also reveal secondary faulting within the subducted Cocos plate on parallel faults, with ruptures both up and down dip. The largest (*M* 6.1) aftershock occurred on 23 September 2017, and was a shallow, onshore event that had its own aftershock sequence. Ortega *et al.* (2019) studied the ground motion of the *M* 8.2 earthquake and found a high attenuation in central Mexico, Oaxaca, and Chiapas. They also studied the subsequent events and found that not all of them were aftershocks due to their different rupture styles (Ortega *et al.*, 2019). Sahakian *et al.* (2018) analyzed ground-motion models for the Tehuantepec and Mexico Puebla earthquakes and determined that more sophisticated basin effects need to be incorporated to improve hazard and risk assessment in Mexico and any country.

Tehuantepec earthquake damage in the Juchitán area

Structural damage of houses and other buildings due to the Tehuantepec earthquake has been previously analyzed (Pozos-Estrada *et al.*, 2019; Fuentes *et al.*, 2019). The majority of the damage in the state of Oaxaca due to the Tehuantepec earthquake impacted either self-constructed houses or historical buildings (Pozos-Estrada *et al.*, 2019). About 65,000 houses were damaged in Oaxaca, and 41% of the total were cataloged as a total loss. The majority of housing in Mexico, both in urban and rural areas, is built using masonry-based structural systems. These types of structures in tectonics settings, such as the one in our area, present a high seismic risk (Godínez-Domínguez *et al.*, 2021).

Figure S2 shows the distribution of damage caused during September 2017 overlapping the topography map of the study area. A correlation with the location of rivers seems apparent. For example, Tehuantepec, Juchitán, and both Santo Domingo and La Union are located near the Tehuantepec, Los Perros, and Chicapa rivers, respectively, and show higher damage compared to Salina Cruz despite being a larger city. Many houses and historical buildings in Juchitán were damaged due to the seismic activity following the Tehuantepec earthquakes, obtained from the Atlas Nacional de Riesgo (CENAPRED *et al.*, 2017). In this study, we also compare the mapped damage with the distribution of our H/V spectral ratio curves obtained at every node location.

Subsurface geology in Juchitán

The geology of the Juchitán region comprises a crystalline basement of igneous origin covered by a soft sedimentary alluvial fan from the quaternary deposited by rivers passing through the surrounding mountains. Because of the subducting Cocos plate, granitic and granodioritic igneous bodies and adjacent metamorphic rocks are observed in the nearby mountains (Sedesol, BC Consultores Ambientales y de Riesgos S.C., 2012). These remnants of ancient volcanic environments surround the Juchitán region, but there is only one active volcano (El Chichón) approximately 215 km northeast of Juchitán.

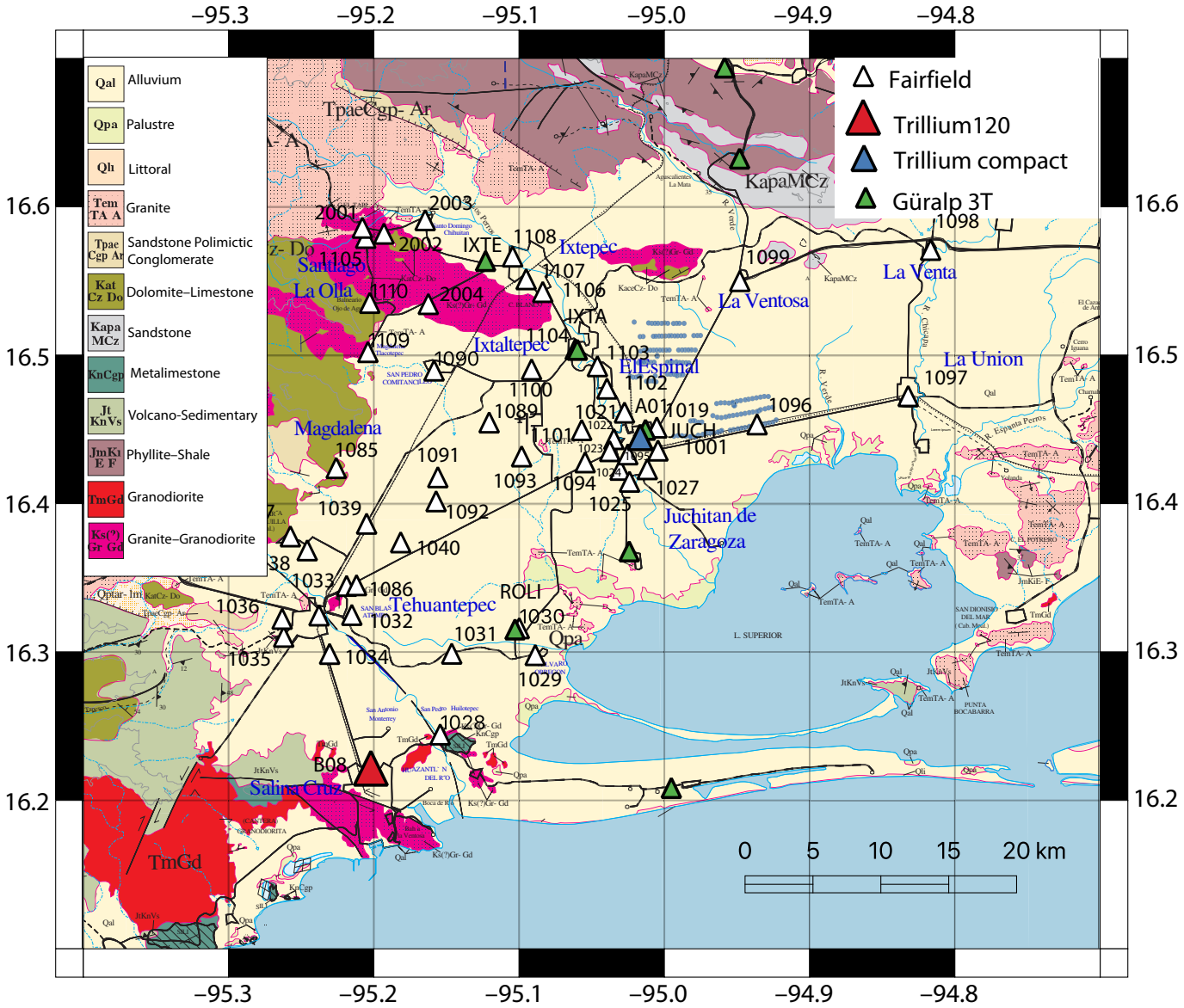

Figure 3. Geology map of the study region. Geological formations can be identified on the map by color; tan indicates unconsolidated sediments (alluvium), dark green indicates limestone and dolomite, red indicates granodiorite, pink indicates granite, and granodiorite, light green indicates volcano-sedimentary, mauve indicates phyllite schist, and gray indicates meta-limestone (modified geological map from Mexican Geological Society [SGM]). The triangles represent seismometer locations, and dots represent drilling sites. The color version of this figure is available only in the electronic edition.

The Juchitán area is composed of different types of sediments (clay and sandstone deposited at the end of the Cenozoic era) on top of the igneous basin (Instituto Nacional de Estadística, Geografia e Informatica [INEGI], 2020). Figure 3 shows a geology map underneath the nodal network. The geology and lack of public awareness in construction procedures for this type of soil may be responsible for the destruction and strong site effects experienced in the region. The differences in the soil composition, as well as variations in the thickness of the sedimentary layer from place to place, could create various frequencies of resonance and site amplification making this a suitable place to conduct an H/V analysis.

Our work builds upon previous studies to analyze the nature of damage under the array. In 2013, the Departamento de Mecanica de Suelos, FSF Ingeniería México conducted a geotechnical study in the neighboring geology of Juchitán and El Espinal to map the soil's characteristics as a function of depth. In their study, conducted prior to the construction of a wind farm consisting of 132 turbines by Eolica del Sur México, they found that the soils in this area are of alluvial origin and composed of detrital sediments, specifically sand and lime clayish sediments. FSF Ingeniería Mexico drilled in the area and did not find solid rock at the top 30 m in near Juchitán (Fig. 3). However, the soils are increasingly consolidated with depth and show low plasticity (FSF Ingenieréía México, 2013).

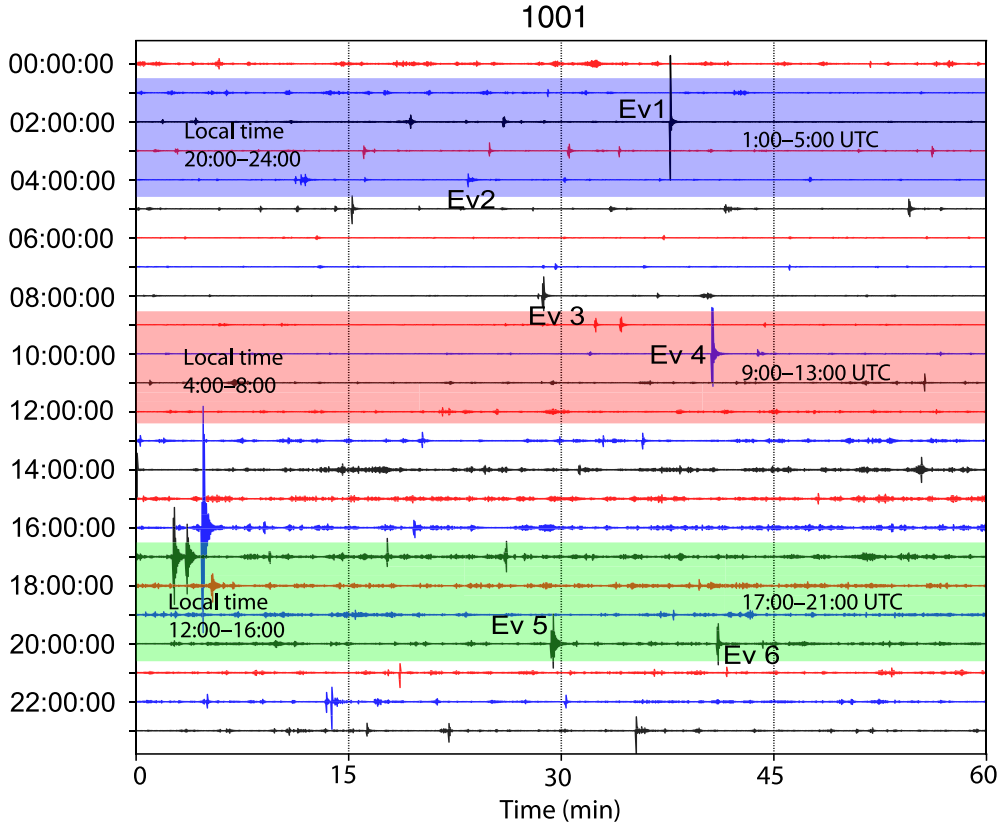

Figure 4. 24 hr plot of the vertical component for node station 1001 recorded on 7 October 2017. The shadow areas illustrate the three time periods to be used in the analysis (UTC: 1:00–5:00, 9:00–13:00, and 17: 00–21:00 and local time: 20:00–24:00, 4:00–8:00, and 12:00–16:00). The color version of this figure is available only in the electronic edition.

RAPID-RESPONSE DEPLOYMENT DATA AND OTHER DATA

Initially, a nodal network of 51 UTEP-owned 5 Hz Magseis Fairfield Z-Land Generation two 3-C seismometers was deployed in October 2017 for 22 days (1–22 October) to capture the spatiotemporal evolution of aftershocks following the Tehuantepec earthquake (Fig. 1). The nodal deployment had a nominal spacing of around 3 km and covered the coastal plains to the mountainous regions near Juchitán. It was one of the first deployments of nodes used for an aftershock study outside of Oklahoma (Kim and Keranen, 2018). Although the cutoff frequency of the nodes is 5 Hz, laboratory and field data tests have shown that the nodes are capable of reliably recording frequencies below 1 Hz and likely down to 0.15 Hz (e.g., Ringler *et al.*, 2018). In this article, we explored the capabilities of these instruments to compute H/V spectral ratio calculations to quantify site effects after great earthquakes.

Along with these instruments, ten Nanometrics Trillium 120 PA broadband seismometers with Reftek RT130 data loggers were deployed in early October 2017 for six months to record the aftershock seismicity in the offshore Tehuantepec epicentral region (Fig. 1). These instruments were borrowed from Incorporated Research Institutions for Seismology Portable Array Seismic Studies of the Continental Lithosphere. UNAM had previously deployed a Nanometrics Trillium Compact broadband at the University of Juchitán to fill gaps of SSN network in the area. The position of this and previous deployments in the area are shown in Figure 3 along with the geology map.

We recovered complete data from 50 out of 51 nodes (98% recovery). Even though some nodes were recording for the entire 22 days, for this study, data from only 15 days (6–20 October) was used when all of the nodes were recording. The earthquake data used here comes from the seventh day of the nodal deployment and consisted of at least 180 s of the six seismic events described in Table 1, derived from the SSN catalog. To illustrate the amount of seismic activity, Figure 4 shows a sample seismic trace for the vertical component of station 1001 for the six events. The record also illustrates the robust nature of the aftershock sequence and the high-quality recordings derived from a typical node station.

The Tehuantepec isthmus proves to be a very unusual, complex tectonic region and has been studied in the recent past. From August 2007 to March 2009, the Veracruz Oaxaca deployment (VEOX) consisted of 45 sensors that spanned 300 km. The Oaxaca section of this network started near the Isthmus of Tehuantepec to study the tectonics of the region (e.g., Kim *et al.* 2011; Melgar and Pérez-Campos, 2011). Broadband data from that deployment was also utilized because 5 out of the 45 Güralp 3T stations overlapped the area of interest as shown in Figure 3. We include this data in our analysis, and it allows us to directly compare results obtained from broadband recordings with the ones obtained from the nodal data.

H/V METHODS

The H/V approach estimates the ratio between the Fourier amplitude spectra of the horizontal (H) to vertical (V) components of the ambient noise vibrations recorded at one single station (e.g., Nogoshi and Igarashi, 1971; Nakamura, 1989). This technique uses noise coming from different ambient

TABLE 1
Table for the Six Earthquakes Used in the Earthquake Horizontal-to-Vertical Spectral Ratio (EHVSR) Approach

Description	Magnitude	Latitude	Longitude	Depth (km)	Reference	Time UTC (hh:mm:ss)
Ev1	4	16.4667	−94.9228	26.9	10 km east from Union Hidalgo, Oaxaca	02:37:38
Ev2	4.2	15.4170	−94.6645	17.7	102 km southeast from Salina Cruz, Oaxaca	04:23:09
Ev3	4	16.4117	−95.0820	56.5	7 km southeast from Juchitán de Zaragoza, Oaxaca	09:34:08
Ev4	4.1	16.5115	−95.0397	76.9	9 km southeast from Ixtepec, Oaxaca	10:40:33
Ev5	4.6	16.6998	−95.2142	92.3	19 km northeast from Ixtepec, Oaxaca	20:29:02
Ev6	4	16.4500	−95.0858	77.6	7 km west from Juchitán de Zaragoza, Oaxaca	20:40:59

vibration sources (wind, ocean, and anthropogenic sources) to identify seismic resonance frequency (Lane *et al.*, 2008), and it can also reflect different types of seismic waves (body and surface waves) that are generated. The frequency of the signals can reflect the source type (<1 Hz from natural sources and >1 Hz from anthropogenic sources) (Site EffectS Assessment using AMbient Excitations [SESAME] European research project WP12-Deliverable D23.12, 2004). Bonnefoy-Claudet *et al.* (2006) performed numerical simulations of H/V ratios and illustrated that the use of shallow noise sources near a receiver allows for the determination of one fundamental resonance frequency. Variations of the H/V method have been developed, and we explore several of these approaches subsequently.

H/V spectral ratio using continuous data

We decimated the seismograms recorded with the nodes from 1000 to 200 samples per second to import the data into the software Grilla that comes with the digital tomograph TROMINO (see Data and Resources), an instrument that is standardly used to conduct H/V analysis. We reviewed the data quality of H/V curves over 24 hr. Figure 5 shows an example of the stability of the spectral ratio measurements and the respective H/V curve calculated for the 24 hr of day 6 in a node (station 1001) located in Juchitán. To investigate the variations of the H/V spectrum throughout the day, we divided the data set into the following three equally spacing periods: 4:00–8:00, 12:00–16:00, 20:00–24:00 local time or 9:00–13:00, 17:00–21:00, 1–5 UTC. We then conducted an H/V analysis using continuous data from the same three periods and from 14 October, which was randomly selected to identify the time in the day at which the measurements were more stable. To do this, we determined the maximum H/V amplitude in the different periods and visually analyzed the nature of peaks to see if they come from stratigraphic origin. We used a 50 s time window and a Konomachi algorithm with a *b*-value of 40. We visually inspected the frequency range between 0.2 and 70 Hz, finding that all of the H/V maxima were between 0.2 and 20 Hz.

MHVSR using nodes

We utilize the Geopsy software to calculate the H/V spectral ratio curves using microtremors and apply an antitriggering algorithm to the data to avoid earthquakes among other transient signals (Wathelet *et al.*, 2020). We investigate the variability of H/V curves using noise throughout the day within the 15 days by calculating the curves for the before-mentioned three time periods. Because of the robust aftershock sequences collected during the RAPID network deployment, we applied a short-term, long-term (STA/LTA) antitriggering algorithm to avoid the earthquakes within the designated time windows. We explored a variety of parameters for the H/V calculations: time windows of 30, 50, and 100 s. We settle with 50 s windows and STA/LTA of 1 s/ 25 s with a minimum of 0.2 and a maximum of 4 for our calculations along with a bandwidth of 40 using the Konno and Omachi (1998) algorithm. These parameters are sufficient to remove transient local events (Chen *et al.*, 2008). The frequency range was chosen to 0.2–20 Hz resulting from the analysis of continuous data; we note that 43 stations were deployed on the same type of alluvium and expected H/V peaks within that range. Figure S3 shows an example of the Geopsy window used for calculating the spectral ratio in 1001. The figure allows us to see that the main arrivals of Ev1 (randomly selected) were avoided in all the three components (N, E, and Z) when applying the previously mentioned STA/LTA ratio. We also computed the average of all H/V curves across the 15 days for the chosen time periods.

MHVSR using broadband data

Data from three types of broadband sensors were used to calculate the H/V curves: Trillium 120 for our station in Salina Cruz, Nanometrics Trillium Compact for the temporal UNAM station deployed in Juchitán, and Güralp 3T from VEOX deployed in Ixtepec, Juchitán, and Ixtaltepec. We used four hours of data from 1–5 a.m. UTC in October 2009 and applied the same parameters (50 s windows, STA/LTA of 1/25, and the bandwidth of 40) as the ones applied to the nodes using Geopsy to compare the average behavior of the H/V curves across instruments. These data were recorded from different years (2008, 2017, and 2018), which allow us validate the results from the nodes.

Earthquake horizontal-to-vertical spectral ratio (EHVSR)

We also explored the H/V curves in the area of Juchitán obtained when using the six seismic events from Table 1 to

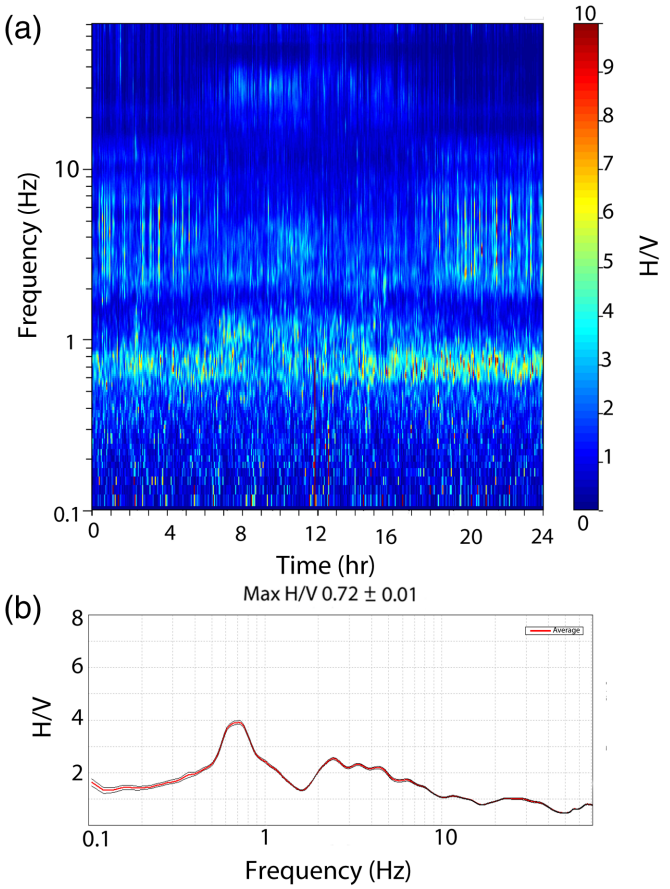

Figure 5. (a) Horizontal-to-vertical (H/V) stability spectrum of station 1001 for day 24 hr of day six (local time), showing the stable spectral peaks within his time window at this station. (b) H/V spectral ratio curve (red line) and the standard deviation (black line) using Grilla for same day, again illustrating the stable spectral peaks at this station. The color version of this figure is available only in the electronic edition.

compare the results with those calculated with noise in Juchitán (e.g., Lermo and Chávez-García, 1993; Laurendeau *et al.*, 2018). We utilized at least 180 s of data and computed the H/V spectral curve using a time window of 50 s. Table 1 shows the events that were used to estimate the EHVSR curves.

Site amplification (standard spectral ratio)

Site amplification was computed following the methodology by Borcherdt (1970). Specifically, we select data from 7 of 51 possible stations as possible Green's functions (1085, 1105, 1109, 1110, 2001, 2002, and 2004), using stations that deployed on hard rock sites (not in alluvial sediments) as the denominator in the deconvolution, using our geological map to assist with the classification of possible hard rock sites (Fig. 3). Thus, instead of one reference site, we have seven reference sites. Because we did not have the events fully characterized (magnitude, focal mechanism, accurate depth, etc.) and because we use the entire seismogram (not individual phases), we do not correct each spectra for geometrical spreading using the distance between the event and the different station paths (e.g., Bonilla *et al.*, 1997). We thus, assume that the geometrical spreading is averaged out over all events and Green's functions for each station. Regardless, our approach allows us to calculate the relative amplification of the remaining 43 sites that were deployed in sediments represented by the light color in Figure 3. After obtaining the amplification for each station considering the six events from Table 1, we calculated the root mean square (rms) spectral amplitude in the frequency ranges 0.2–2 Hz, 4–8 Hz, and 8–16 Hz, and then we average those results for the seven reference stations. We did this for the vertical (Z) component alone and for a combination of both horizontal components (N and E).

Contour maps

We interpolate our frequency of resonance and amplification results to create various contour maps for our results using MATLAB and the Bayesian kriging algorithm (e.g., Schultz *et al.*, 1998). Kriging allows for errors to be incorporated into the interpolation and stabilizes the interpolation when close stations have different results. We removed the mean of the data before the interpolation and then added the mean value, generating a smooth surface that matches the original data points. We also used a lateral influence for each station such that the interpolated H/V peak frequency value goes to the background.

RESULTS

H/V analysis using continuous data

As discussed in the H/V methods section, we chose 14 October to explore the H/V curves using 12 hr of continuous data divided into the same three periods. The standard Grilla software (see Data and Resources) was also used for this analysis to identify the period at which the standard deviation is lower. The results, shown in Table 2, determine the frequency at which we have the maximum H/V ratio for the different periods of the day. In general, the period does not significantly vary the resulting pattern of frequencies, and the H/V maximums generally range from 0.2 to 20 Hz. However, stations 1099, 1035, and 1110 have a lot of variation (Fig. S5). In the contour maps of the H/V peaks (Fig. 6), we note similarities in the overall pattern with the continuous data for one day and 15 days when only using noise. We also looked at the pattern of the standard deviation in Figure S5, suggesting that some sources of probably industrial origin at that particular time were interfering and causing the fluctuations.

MHVSR using noise

2250 H/V curves in the frequency range of 0.2–20 Hz were obtained for all nodes across the three-time periods (1:00–5:00, 9:00–13:00, and 17:00–21:00 UTC) for the 15 days of data analyzed. These resulting curves were averaged to get an idea of the overall behavior of H/V in each site. Figure S4 shows a

TABLE 2
Horizontal-to-Vertical (H/V) f_0 for Three Periods during Day 14 Showing Similar Behavior for the Majority of Stations during the Different Times

Station	Latitude	Longitude	H/V Peak Frequency ± Standard Deviation (Hz) 1–5	H/V Peak Frequency ± Standard Deviation (Hz) 9–13	H/V Peak Frequency ± Standard Deviation (Hz) 17–21
1001	16.43570	−95.00359	0.73 ± 0.25	0.68 ± 0.19	2.34 ± 1.09
1019	16.45122	−95.00439	0.59 ± 0.02	0.58 ± 0.08	0.61 ± 0.1
1021	16.46129	−95.02665	0.58 ± 0.03	0.59 ± 0.02	0.59 ± 0.05
1022	16.44342	−95.03397	0.75 ± 0.02	0.75 ± 0.04	0.73 ± 0.04
1023	16.43530	−95.03678	0.93 ± 0.05	0.91 ± 0.65	1.08 ± 0.02
1024	16.42272	−95.02966	1.12 ± 0.02	1.1 ± 0.1	1.12 ± 0.03
1025	16.41467	−95.02318	0.89 ±0.03	0.94 ± 0.05	0.98 ± 0.02
1027	16.42314	−95.01095	0.82 ± 0.02	0.82 ± 0.03	0.19 ± 1.01
1028	16.24429	−95.15355	5.38 ± 0.15	5.46 ± 0.07	0.21 ± 4.24
1029	16.29780	−95.08809	1.13 ± 0.25	1.12 ± 0.01	3.75 ± 0.21
1030	16.31590	−95.09910	1.06 ± 0.01	1.06 ± 0.02	1.08 ± 0.01
1031	16.29876	−95.14560	1.52 ± 0.65	1.55 ± 0.04	1.59 ± 0.16
1032	16.32488	−95.21439	2.58 ± 0.03	2.57 ± 0.01	2.55 ± 0.01
1033	16.34448	−95.21799	2.57 ± 0.01	2.58 ± 0.03	2.57 ± 0.02
1034	16.29860	−95.22969	1.76 ± 0.09	1.73 ± 0.06	1.76 ± 0.05
1035	16.31012	−95.26128	15.68 ± 5.76	15.71 ± 0.07	5.31 ± 0.29
1036	16.32224	−95.26236	2.01 ± 0.01	2.04 ± 0.04	2.06 ± 0.04
1037	16.37784	−95.25669	4.96 ± 0.09	4.92 ± 0.04	4.97 ± 0.07
1038	16.36842	−95.24511	2.79 ± 0.02	2.81 ± 0.01	2.74 ± 0.17
1039	16.38637	−95.20422	2.92 ± 0.08	2.97 ± 0.02	2.97 ± 0.23
1040	16.37382	−95.18074	2.22 ± 0.69	9.51 ± 6.4	9.64 ± 0.15
1085	16.42390	−95.22514	14.82 ± 1.01	14.72 ± 0.86	13.65 ± 2.95
1086	16.34492	−95.21115	2.55 ± 0.01	2.55 ± 0.04	2.53 ± 0.03
1087	16.32454	−95.23696	9.27 ± 0.89	9.44 ± 0.26	9.5 ± 0.1
1089	16.45463	−95.11984	5.22 ± 0.47	5.18 ± 0.27	5.39 ± 0.07
1090	16.48964	−95.15775	0.45 ± 1.72	5.73 ± 0.79	5.88 ± 1.75
1091	16.41770	−95.15518	9.95 ± 0.81	10.05 ± 0.59	9.98 ± 0.13
1092	16.40148	−95.15637	1.9 ± 5.81	8.01 ± 2.61	9.44 ± 0.04
1093	16.43175	−95.09747	3.28 ± 0.33	7.98 ± 2.55	3.28 ± 1.54
1094	16.42777	−95.05375	1.24 ± 0.75	1.24 ± 0.85	2.23 ± 0.01
1095	16.43312	−95.02438	0.73 ± 0.03	0.73 ± 0.04	1.08 ± 0.02
1096	16.45335	−94.93537	0.77 ± 0.03	0.77 ± 0.01	0.84 ± 0.02
1097	16.47239	−94.83133	0.51 ± 0.03	0.52 ± 0.01	0.51 ± 0.03
1098	16.57098	−94.81588	0.26 ± 0.01	0.26 ± 0.02	0.26 ± 0.01
1099	16.54996	−94.94724	5.17 ± 2.02	5.29 ± 0.14	5.06 ± 1.9
1100	16.49039	−95.09062	1.89 ± 0.91	0.19 ± 0.65	14.72 ± 0.41
1101	16.44951	−95.05612	1.15 ± 0.02	1.13 ± 0.47	1.15 ± 0.04
1102	16.47746	−95.03874	0.86 ± 0.08	0.86 ± 0.06	0.99 ± 0.04
1103	16.49254	−95.04530	0.72 ± 0.05	0.7 ± 0.04	0.72 ± 0.04
1104	16.50403	−95.06057	0.89 ± 0.56	4.89 ± 0.51	1.19 ± 0.51
1105	16.57909	−95.20483	6.53 ± 2.33	6.53 ± 1.89	8.34 ± 0.11
1106	16.54261	−95.08292	4.08 ± 0.03	4.1 ± 0.07	4.12 ± 0.08
1107	16.55121	−95.09436	5.25 ± 0.03	5.31 ± 0.09	5.36 ± 0.2
1108	16.56649	−95.10365	4.43 ± 0.08	4.4 ± 0.08	4.36 ± 0.03
1109	16.50210	−95.20330	10.75 ± 2.17	10.72 ± 0.05	4.84 ± 5.1
1110	16.53525	−95.20204	19.99 ± 0.66	19.99 ± 1.1	19.99 ± 0.32
2001	16.58591	−95.20711	7.52 ± 0.06	7.51 ± 0.03	7.54 ± 0.66
2002	16.58192	−95.19228	6.13 ± 0.37	5.99 ± 0.08	6.09 ± 0.17
2003	16.59103	−95.16388	3.18 ± 0.08	3.21 ± 0.08	3.18 ± 0.04
2004	16.53446	−95.16171	4.78 ± 0.56	4.8 ± 0.03	4.85 ± 0.06

comparison of the H/V curves using noise calculated from the 12 nearest stations in Juchitán de Zaragoza where the majority of houses were damaged (more than 10,000). We note that the effect of time on the peaks defining the frequency of resonance is clear for stations 1094, 1027, 1102, and 1023 when comparing the H/V behavior for specific times to the average (Fig. S4)

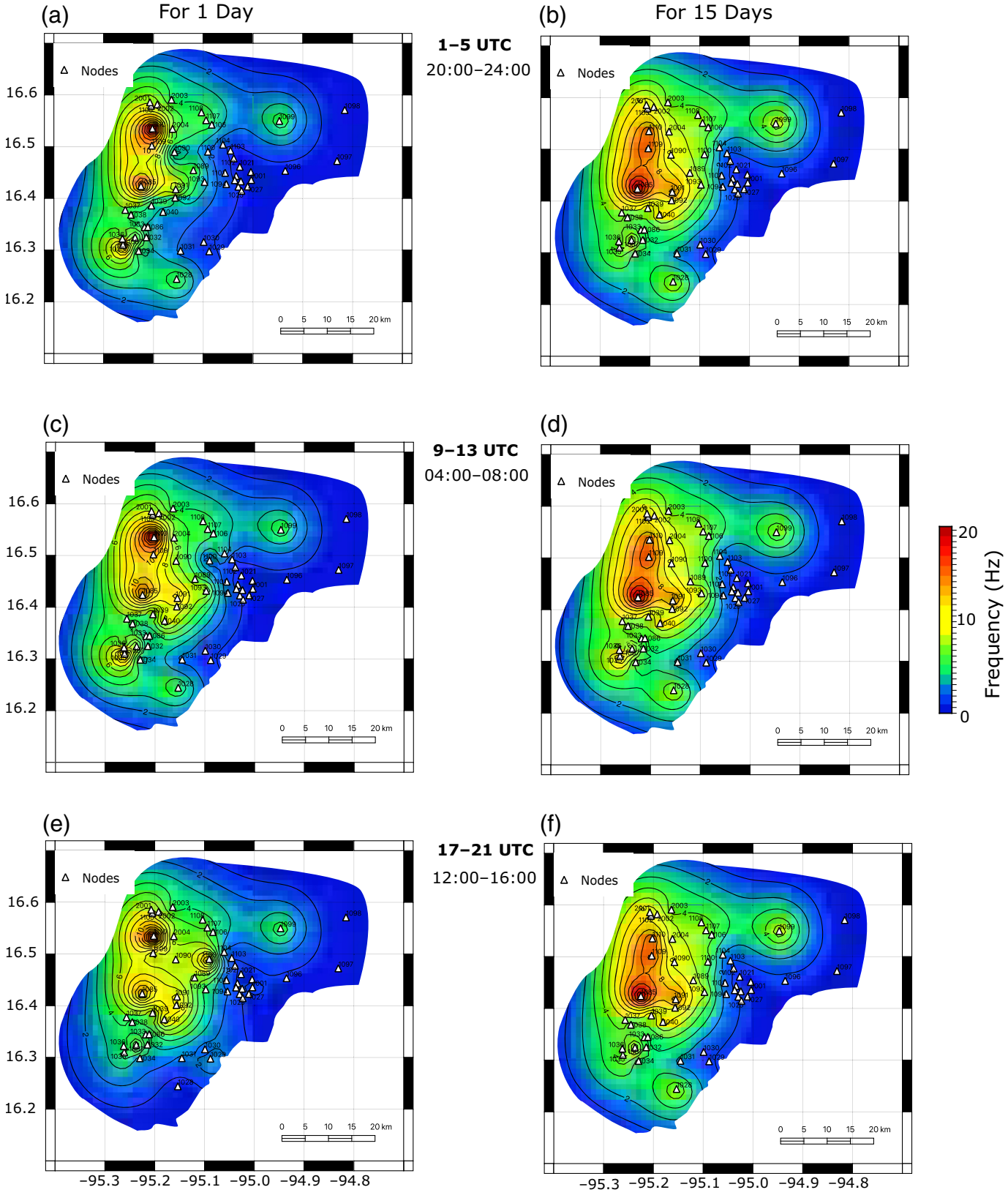

Figure 6. (a,c,e) Contour maps of H/V peak frequency for the three different periods of the day (top: 1–5 UTC; middle: 9–13 UTC; and bottom: 17–21 UTC) calculated for 14 October using all the stations. (b,d,f) Contour maps of H/V peak using all stations, for the three periods averaged over the 15 days. The blue colors represent low frequency values, whereas the red colors represent high frequency values. The color version of this figure is available only in the electronic edition.

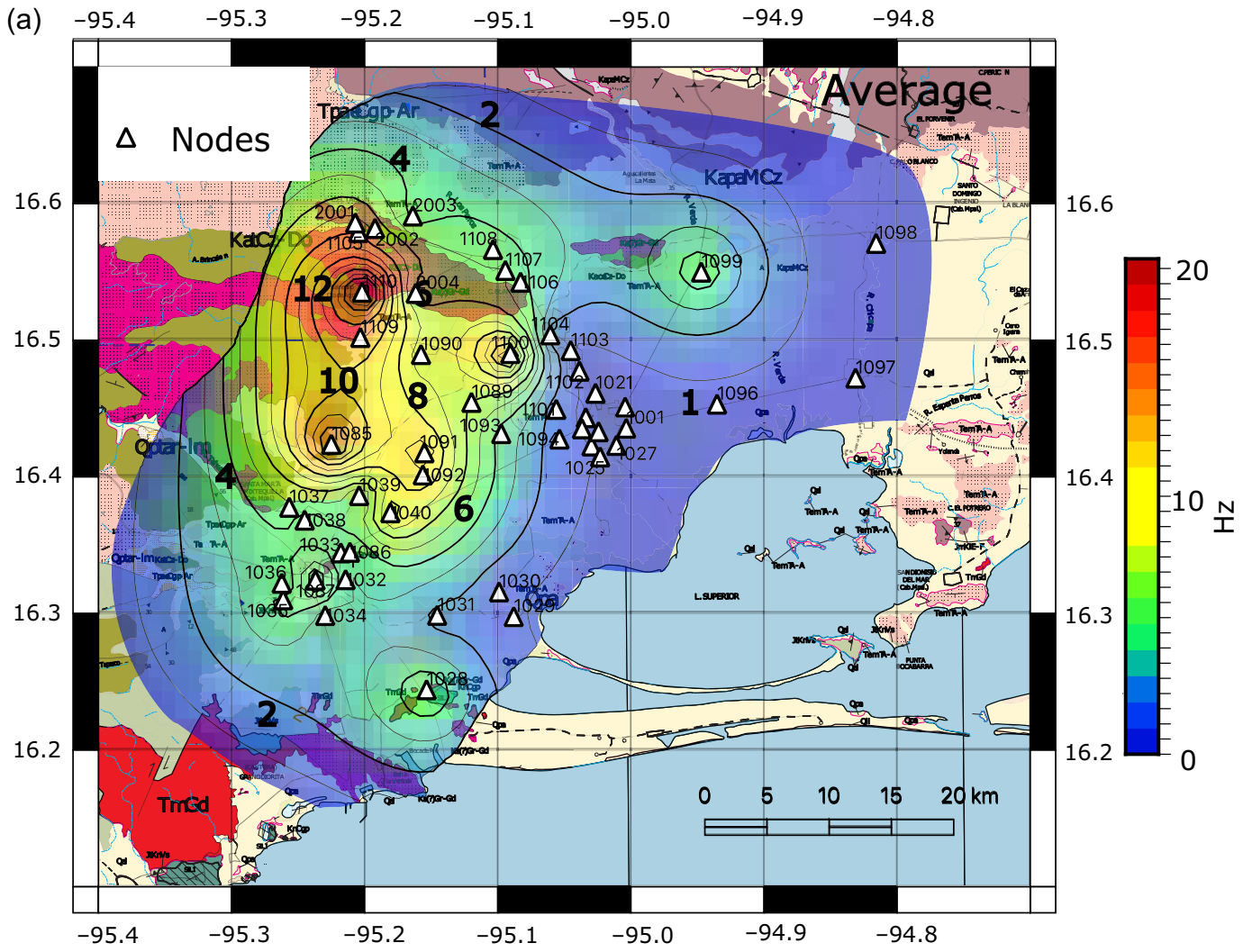

Figure 7. (a) Contour map of average of H/V peak frequencies for 15 days. (b) Average H/V spectral ratio curves calculated from all periods during the 15 days using noise. These graphs are plotted at the same scale and are organized according to their shape and in ascending order for the H/V peak frequency (f_0). The background colors represent the type of material in which they were deployed: tan for unconsolidated sediments (alluvium); dark green for limestone and dolomite; and pink for granite and granodiorite following the Geology Map from Instituto Nacional de Estadística y Geografía (INEGI). The color version of this figure is available only in the electronic edition.

(*Continued*)

in which we see a slight shift to higher frequencies in the time of 17–21 UTC.

Figure 7 presents the average spectral ratio behavior per site of all curves for all times and days. The background colors represent the type of geology underneath each station. We organize the curves according to their shape and in ascending order of frequency of resonance (e.g., Hellel *et al.*, 2010; Panzera *et al.*, 2018; Pacheco *et al.*, 2021). Attention was given to the larger H/V peak frequency that corresponds to the resonance frequency for the majority of stations. Station 1097 has one of the lowest frequencies of resonance, whereas there seems to be an increase of frequencies the closer the stations are to the mountains. We see this in the overall behavior in two directions if we follow 1097, 1096, 1094, and 1092 (Figs. 3 and 7). This same behavior is present in 1019, 1021, 1103, and 1106 stations (Figs. 3 and 7). The presence of igneous intrusions near station 1028 and all the ones surrounding Tehuantepec seems to affect the tendency to higher frequencies as well, which may be related to basin depth fluctuating below the nodes.

The resulting contour maps generated from the average H/V peak frequency values for all days of the deployment and for one day (Fig. 6) for the three time windows showing a low-frequency zone in Juchitán de Zaragoza, La Venta, La Union, and in Tehuantepec a local minimum. Low-frequency zones tend to follow the riverbeds and high-frequency zones the places near the mountains, such as Magdalena and Santiago de la Olla. Our maps show similar overall low- and high-frequency zones despite the use of different time periods. Differences in H/V amplitude and resonance frequencies exist across the array but are stable on different days. Another important result is the amount of data

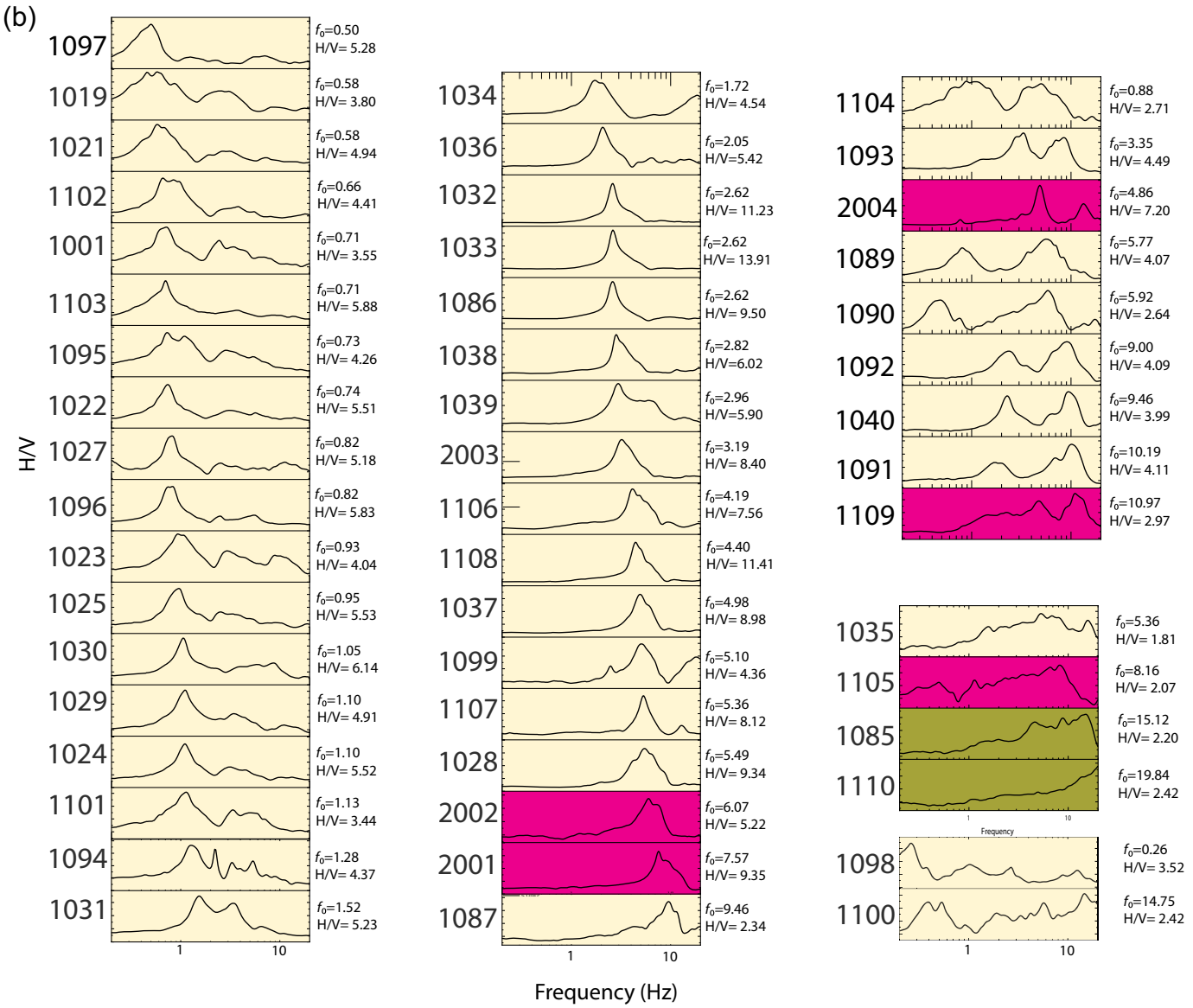

Figure 7. Continued

that needs to be used to identify the low- and high-frequency zones. We did the same H/V analysis for two hours of data and found that the results were similar to those obtained using the average for the fifteen days.

EHVSR results

Figure S6 shows the comparison of H/V curves calculated with six earthquakes and with what is considered noise for the same 12 stations in Juchitán to test consistency. The individual curves obtained with earthquakes change and sometimes the frequency of resonance is difficult to identify, but, when averaged, they show consistent behavior with those obtained for the average H/V using noise. For example, the curve calculated for stations 1023 and Ev2 does not have a well-defined H/V peak at low frequencies, but when it is averaged with the other events, station 1023 shows a low-frequency zone. This same behavior can be seen with station 1022 and Ev2 or with station 1094 and Ev3.

Site amplification

Despite this work focusing mainly on the frequency response of the soils, we also calculated the relative amplification under the array. We showed the average relative amplification in the vertical and horizontal components for all stations deployed on top of sediments. We use all six earthquake recordings collected on seven stations (1085, 1105, 1109, 1110, 2001, 2002, and 2004) representing a different type of geological formation as the denominator in the deconvolution. Using these results, we

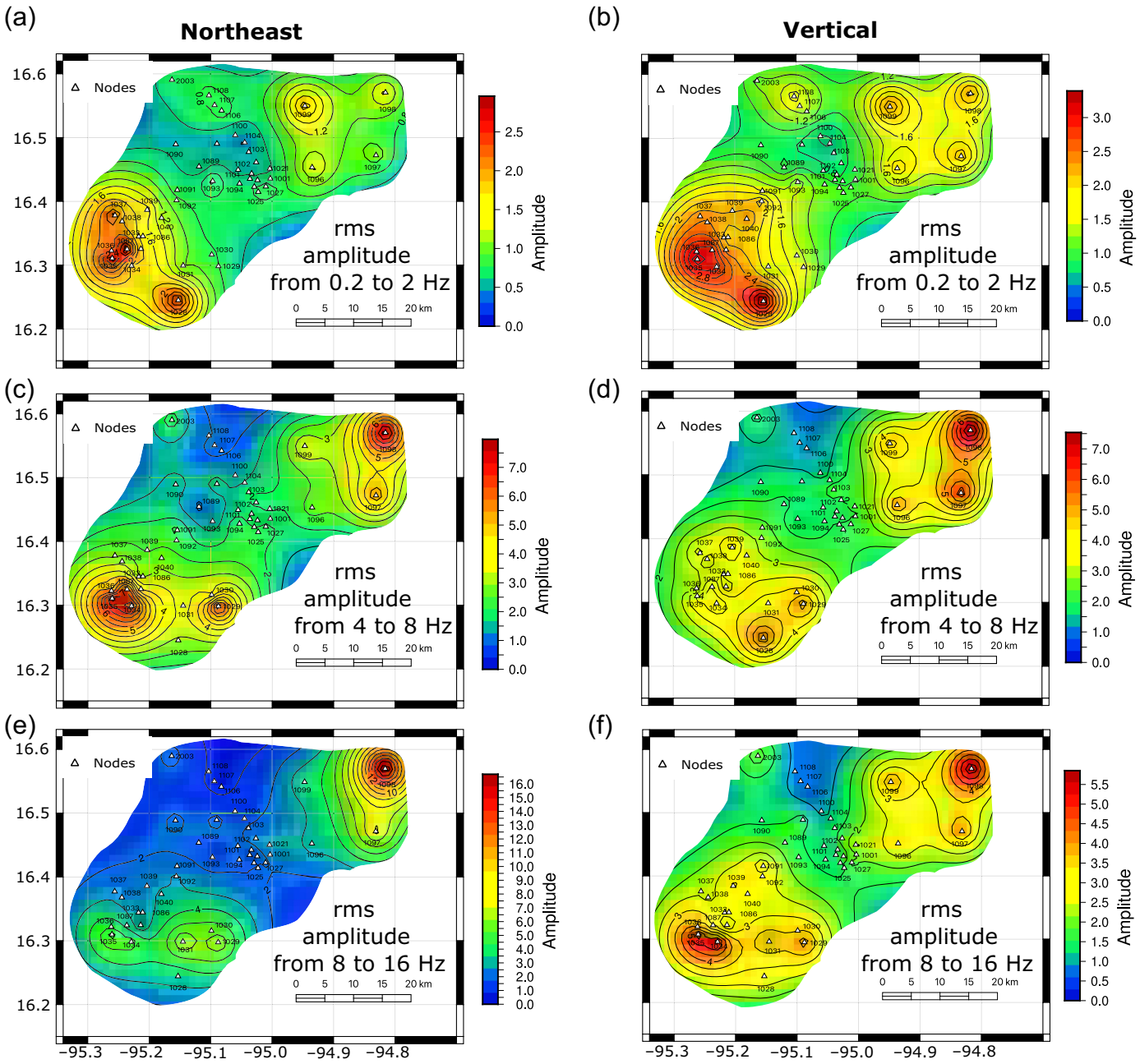

Figure 8. (a,c,e) Contour maps of the average root mean square (rms) relative amplification calculated for the six earthquakes data for northeast component for three bins top from 0.2 to 2 Hz, middle from 4 to 8 Hz, and bottom from 8 to 16 Hz. (b,d,f) rms amplification for the vertical component calculated for the same intervals as in the northeast. The color version of this figure is available only in the electronic edition.

computed the rms amplitude (0.2–2 Hz, 4–8 Hz, and 8–16 Hz) for both vertical and northeast components of all the curves computed in the nodal array (Fig. 8). Figure 8 shows a low-amplification zone in Juchitán and a high amplification surrounding the area of Juchitán. The low amplification in Juchitán corresponds to the low frequencies with MHVSR results (Figs. 6 and 7). However, in the southern region of the study (near station 1034 and near the city of Tehuantepec), we have high amplification with low frequencies.

MHVSR comparison between nodes and broadband stations

We selected and compared results obtained with three different brands of sensors. In Figure 9, we plotted the MHVSR curves for the broadband stations A01, B08, ROLI, IXTE, JUCH, and IXTA along the MHVSR curves obtained for the neighboring nodes. All H/V curves were calculated from 1 to 5 UTC, but with data from different dates. The Güralp 3T data were from 4 October 2008, Trillium 120 data from 21 November 2017, Trillium Compact data from 2 February 2008, and Magseis

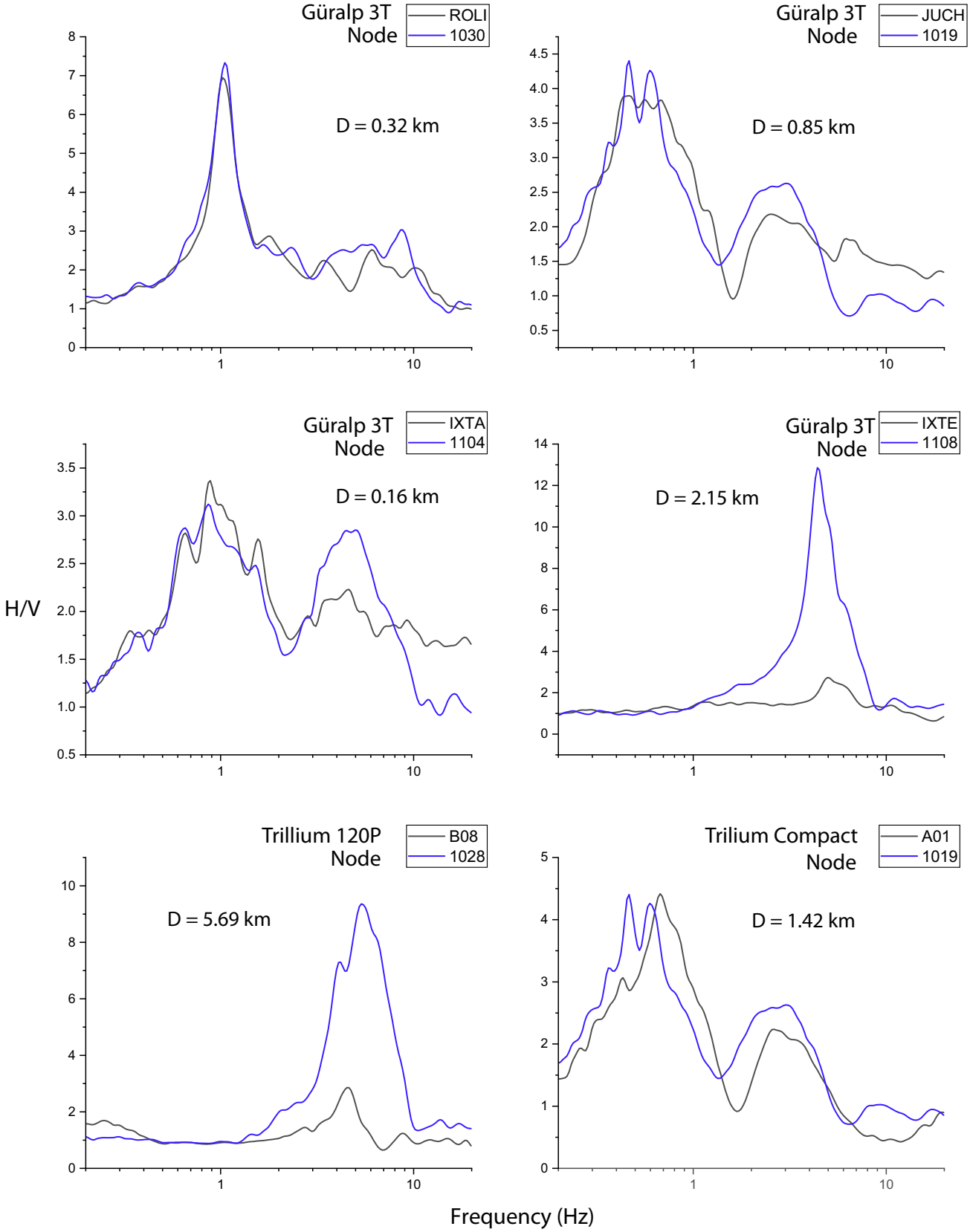

Figure 9. H/V spectral ratio computed for nodes (blue lines) and broadband (black lines) stations. Nodal data are from 7 October 2017, Trillium 120P data from 21 November 2017, Trillium Compact data from 2 February 2018, and Güralp 3T data from 4 October 2008. All curves used data from 1 to 5 UTC. The comparison of stations is based on proximity to nodes (D). Nodes and broadbands showed similar results. The closest distance between the nodes and broadbands is 0.16 km, and the farthest is 5.69 km. Note that stations with D >2 km deviate in amplitude and may shift slightly in peak frequency. The color version of this figure is available only in the electronic edition.

Fairfield node data from 7 October 2017. The comparison shows similarities between the various sensor types. For example, ROLI and station 1030 show a very well-defined frequency of resonance around 1 Hz. The two broadband stations located in Juchitán have a frequency of resonance under 1 Hz for both nodes and broadbands, illustrating that Juchitán de Zaragoza is a low-frequency zone. There are also big differences in the H/V amplitudes for the stations that are separated the most, B08 with 1028 and IXTE with 1108. Despite the difference in instrument type (Güralp 3T, Trillium 120, Trillium Compact, and Magseis Fairfield), we found the Fairfield nodes reliable to identify the frequencies of resonance similar to the broadbands and offer a good alternative for H/V calculations with the advantage of portability and easy deployment.

DISCUSSION AND CONCLUSIONS

We deployed 51 Magseis Fairfield three-component 5 Hz geophones in Juchitán de Zaragoza, Oaxaca, from 1 October 2017, for 22 days, as part of an NSF-funded RAPID seismic deployment conducted shortly after the 8 September 2017 **M** 8.2 Tehuantepec earthquake and after the shallow (10 km depth) **M** 6.1 extensional earthquake. In this study, we explored the capabilities of Fairfield nodal data to identify the frequency of resonance when applying the H/V spectral ratio approach and found that the nodes are capable of detecting resonant frequencies as low as 0.2 Hz. The Fairfield nodes' portability offers a multipurpose tool for both fast generation of site-effect maps and recording of aftershock sequences. These instruments can provide useful information to be used by engineers to understand the hazards caused by earthquakes in regions with high risks, for example, those close to subduction zones, such as Juchitán and the surrounding areas. Thus, we conclude that the nodal instruments have the potential to be used not only for aftershock location but also for future hazard mitigation projects.

The Isthmus of Tehuantepec is known for its powerful winds, particularly La Ventosa (which translates to English as "the windy place"), located in the Juchitán region. Mexico has 54 wind farms, and La Ventosa has the potential to generate 60% of the country's wind capacity (Asociación Mexicana de Energía Eólica [AMDEE], 2017). The presence of turbines in the region has to be taken into consideration as a source of industrial noise. Because of this, we wanted to avoid this source of noise when choosing the natural frequency because three of our stations were deployed near or in the middle of wind farms. To ensure that the main contribution to the curves came from the site itself and not spurious picks of industrial origin, we utilized and analyzed the data from these seismic stations located near La Ventosa to investigate whether we could see similar signals in the surrounding stations near Juchitán. To identify the industrial noise, we computed a power spectral density (PSD) analysis in the three components as recommended (SESAME, 2004). Figure 10 shows (PSD) results for La Ventosa and one station in Juchitán for the different periods from which we conclude that there is an effect from the industrial noise at station 1099 La Ventosa for two time periods (1–5 and 17–21 UTC), but it is not present in the ones from Juchitán. Furthermore, the spectral peak at 2.5 Hz appears strongly in 1–5 UTC and 17–21 UTC time windows, but not in 9–13 UTC time window, suggesting that the source of the peak may originate from wind turbines.

We compare the H/V curves calculated for nodal data to the ones calculated for broadband data from different years but the same period in the day before and after the deployment to ensure that no industrial noise nor aftershocks were considered. We learned that the nodes and broadband instruments prove to be a useful tool to derive the H/V spectral ratios; we found that they offer similar H/V results to broadband data over a frequency range of 0.2–20 Hz and give us enough information to distinguish between zones of high and low resonance frequencies (even lower than 1 Hz). Similar behavior was observed in the region regarding the period of the measurements, which makes it clear that despite a large number of aftershocks, our frequency and amplitude measurements are robust.

Specifically, we used several H/V approaches to determine the resonance frequencies and site amplification across the nodal array and correlate results with the geology of Juchitán and its surroundings. The resulting contour maps of the H/V peak frequency show Juchitán de Zaragoza as a low-frequency zone. We found that regions with high frequencies of resonance correspond to zones with high elevation due to the presence of igneous rocks. We found an apparent connection between river beds, local geology, and damage zones in the study area, where thick sediments underlie zones of significant damage. Interestingly, Juchitán de Zaragoza exhibits low resonance frequency and low amplification, as illuminated in Figures 6–8.

When comparing the average H/V results to the local geology and damage (Fig. S2), we illustrate a correlation with the river beds despite the number of houses. For example, we see less damage in Salina Cruz than in Juchitán. Significant differences exist across the array, highlighting a possible correlation between low frequency and damage in this region. In our study area, there appears to be an inverse relationship between damage and frequency. We found that Juchitán city, with more than 10,000 houses heavily damaged, corresponds directly to the lowest resonance frequency values (Figs. 6 and 7), but almost all the damage was found next to riverbeds, which match the dependency presented in the contour maps.

DATA AND RESOURCES

This article results from a binational (American and Mexican) project; all the information utilized is publicly available. Most of the seismic data used in this study were collected as part of a National Science Foundation (NSF) funded RAPID response network using Incorporated Research Institutions for Seismology (IRIS) Portable Array Seismic Studies of

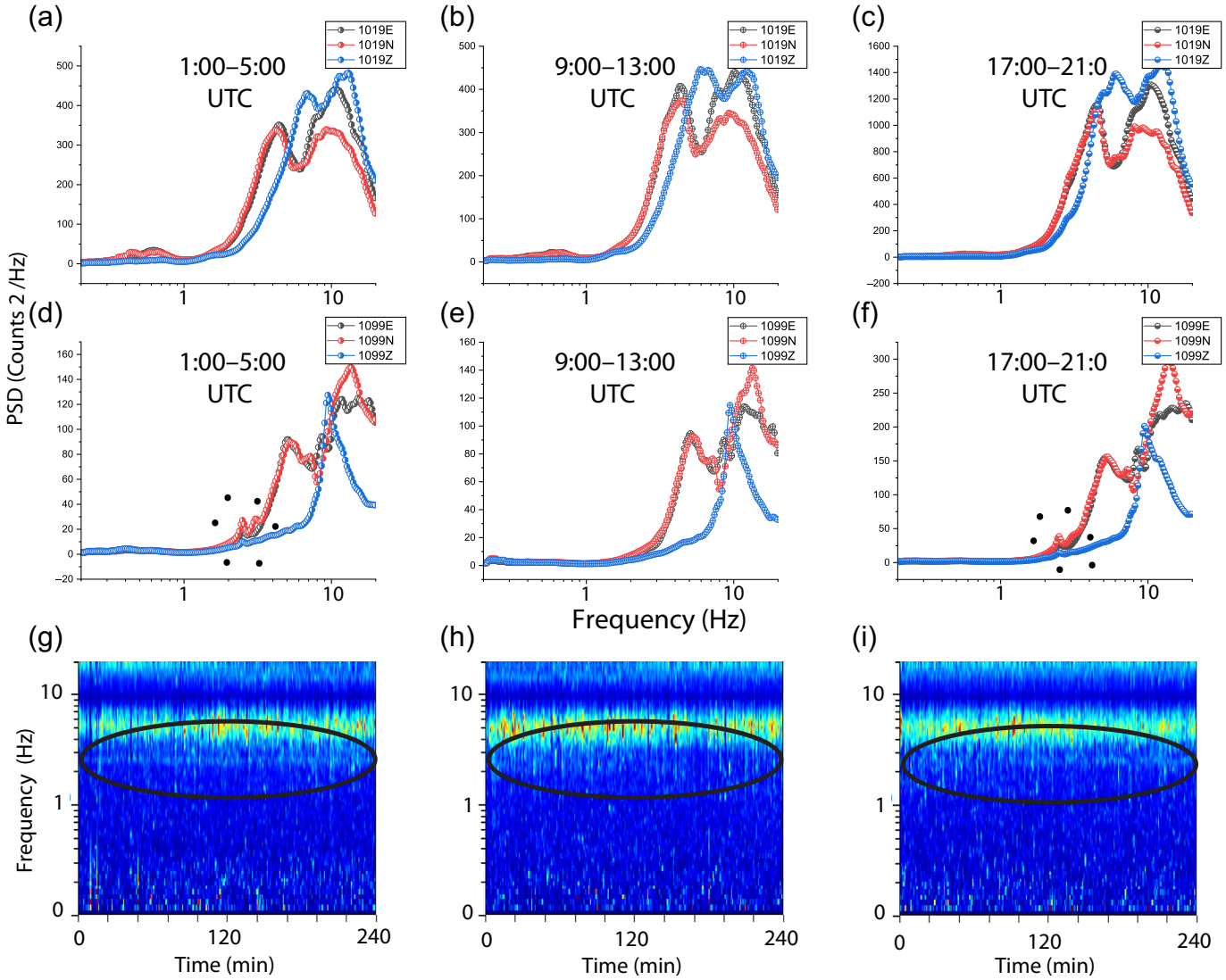

Figure 10. H/V power spectral density (PSD) graphs obtained with Geopsy for all three components for station 1019 (Juchitán) and 1099 La Ventosa. (a,b,c) Results for station 1019 for the three time periods. (d,e,f) Results for station 1099 for the same time periods. First peaks at 2.5 Hz on station 1099 should not be considered frequency of resonance because they appear on all three components (Industrial origin) (e.g., the peak close to 2.5 and 10 Hz). On the other hand, the peaks on station 1019 that should be considered on the low-frequency range, close to 0.5 Hz. (g,h,i) H/V stability spectrum of station 1099 (La Ventosa) for the same time windows. The black ovals illustrate the spectral peak at 2.5 Hz that appears strongly in 1–5 UTC and 17–12 UTC, but not in 9–13 UTC, suggesting the source of the peak may originate from wind turbines. The color version of this figure is available only in the electronic edition.

the Continental Lithosphere (PASSCAL) broadband seismometers and Magseis Fairfield nodes owned by The University of Texas at El Paso. Data can be obtained from the IRIS Data Management Center available at https://www.iris.edu (last accessed August 2020). The remainder of the seismic data was collected by the Servicio Sismológico Nacional (SSN). Data can be obtained from doi: 10.21766/SSNMX/SN/MX and doi: 10.21766/SSNMX/EC/MX (last accessed September 2021). The geological characteristics of Juchitán were obtained from reports created by Secretaría de Desarrollo Social (SEDESOL), available at https://www.oaxaca.gob.mx/proteccioncivil/atlas-de-riesgo/ (last accessed December 2020), and FSF Grupo Ingeniería, available at https://consultaindigenajuchitan.files.wordpress.com/2015/01/estudio-gotecnico-pe-eolica-del-sur.pdf (last accessed December 2020). We used statistical reports of the number of houses damaged in Oaxaca from Secretaría de Desarrollo Agrario, Territorial y Urbano (SEDATU), and Centro Nacional de Prevención de Desastres (CENAPRED), via the platform Atlas Nacional de Riesgos at https://es.scribd.com/document/423564674/Atlas-Riesgos-Naturales-Juchitan-Oaxaca (last accessed December 2022). The Geology map of Juchitán was downloaded from Instituto Nacional de Estadística, Geografia e Informatica (INEGI), available at https://www.inegi.org.mx/app/mapas/ (last accessed December 2020), but modified to suit our interest region. Some maps were created with Generic Mapping Tools version 6.0.0, available at www.soest.hawaii.edu/gmt (last accessed April 2022) (Wessel and Smith, 1998) and QGIS software version 3.12 (https://www.qgis.org/en/site/, last accessed April 2022). All seismogram plots and frequency content plots come from either ObsPy version 1.2.1, available at https://pypi.org/project/

obspy/ (last accessed December 2020) (Beyreuther *et al.*, 2010) or Geopsy version 3.2.2 (SESAME, 2004), available at https://www.geopsy.org (last accessed December 2020). This article would not have been possible without the use of all the aforementioned sources and software. Six figures were included as supplemental material to enrich the content and flow of this article. The other relevant data to this article are available at https://www.tromino.it (last accessed April 2022).

DECLARATION OF COMPETING INTERESTS

The authors acknowledge that there are no conflicts of interest recorded.

ACKNOWLEDGMENTS

Solymar Ayala Cortez was supported by Consejo Nacional de Ciencia y Tecnología (CONACYT). A Centro de Investigación Científica y de Educación Superior de Ensenada (CICESE) internal grant supported Hector Gonzalez-Huizar. The authors also want to thank the field crews from The University of Texas at El Paso (UTEP), Universidad Autónoma de Ciudad Juarez (UACJ), and Universidad Nacional Autónoma de México (UNAM). The authors also thank the people of Oaxaca who let us deploy instruments on their property. The help received by Javier Corral Jurado, Governor of Chihuahua, was of great importance for providing security for the crew and instruments during their transportation across the country with the support of the Chihuahua state police and the Mexican federal authorities. Similarly, the authors are thankful for the help they received from UACJ authorities in the management of crossing and providing the vehicles to transport the instruments deployed in Juchitán de Zaragoza Oaxaca, México, with the collaboration of Mexican and United States customs. The Servicio Sismológico Nacional (SSN) data were obtained thanks to station maintenance, data acquisition, and distribution personnel. The Servicio Sismológico Nacional (México) earthquake catalog is possible thanks to its personnel and product of the calculations made by its Analysis and Interpretation of Seismic Data group. The rapid-response seismic network (RAPID) deployment was supported by a National Science Foundation Grant (Number 1764426).

REFERENCES

AMDEE (2017). Asociación Mexicana de Energía Eólica, Global Wind Energy Council, available at https://gwec.net/wind-companies-working-to-restore-operations-to-100-after-earthquake-in-mexico/ (last accessed September 2022).

Ammon, C. J., H. Kanamori, and T. Lay (2008). A great earthquake doublet and seismic stress transfer cycle in the central Kuril Islands, *Nature* **451,** no. 7178, 561–565, doi: 10.1038/nature06521.

Beck, S. L., and D. H. Christensen (1991). Rupture process of the February 4, 1965, Rat Islands earthquake, *J. Geophys. Res.* **96,** no. B2, 2205–2221, doi: 10.1029/90JB02092.

Beyreuther, M., R. Barsch, L. Krischer, T. Megies, Y. Behr, and J. Wassermann (2010). ObsPy: A Python toolbox for seismology, *Seismol. Res. Lett.* **81,** no. 3, 530–533, doi: 10.1785/gssrl.81.3.530.

Bonilla, L. F., J. H. Steidl, G. T. Lindley, A. G. Tumarkin, and R. J. Archuleta (1997). Site amplification in the San Fernando Valley, California: Variability of site-effect estimation using the S-wave, coda, and H/V methods, *Bull. Seismol. Soc. Am.* **87,** no. 3, 710–730, doi: 10.1785/BSSA0870030710.

Bonnefoy-Claudet, S., C. Cornou, P.-Y. Bard, F. Cotton, P. Moczo, J. Kristek, and D. Fäh (2006). H/V ratio: A tool for site effects evaluation. Results from 1-D noise simulations, *Geophys. J. Int.* **167,** no. 2, 827–837, doi: 10.1111/j.1365-246X.2006.03154.x.

Borcherdt, R. D. (1970). Effects of local geology on ground motion near San Francisco Bay, *Bull. Seismol. Soc. Am.* **60,** 29–61.

Bravo, H., C. J. Rebollar, A. Uribe, and O. Jimenez (2004). Geometry and state of stress of the Wadati-Benioff zone in the Gulf of Tehuantepec, Mexico, *J. Geophys. Res.* **109,** no. B4, doi: 10.1029/2003JB002854.

Centro Nacional de Prevención de Desastres (CENAPRED) (2018). *Desastres en México*, available at https://www.gob.mx/cenapred (last accessed September 2022).

CENAPRED, Colegio de Ingenieros Civiles de Mexico (CICM), and Sociedad Mexicana de Ingenieria Estructural (SMIE) (2017). Atlas Nacional de Riesgos, available at http://www.atlasnacionalderiesgos.gob.mx/archivo/eventos.html (last accessed April 2022).

Chen, Q., L. Liu, W. Wang, and K. He (2008). Seismic hazard assessment with microtremor array observation and computational simulation in the metropolitan Beijing area, *The 14th World Conf. on Earthquake Engineering*, 12–17 October 2008, Beijing, China.

Dougherty, S. L., and R. W. Clayton (2014). Seismicity and structure in central Mexico: Evidence for a possible slab tear in the south Cocos plate, *J. Geophys. Res.* **119,** no. 4, 3424–3447, doi: 10.1002/2013JB010883.

FSF Ingeniereía México (2013). *Estudio geotectnico del terreno para la construccion de un parque eolico formado por 132 generadores*, Scribd, available at https://es.scribd.com/document/388357518/Estudio-Gotecnico-Pe-Eolica-Del-Sur (last accessed April 2022) (in Spanish).

Fuentes, D. D., P. A. Baquedano Julià, M. D'Amato, and M. Laterza (2019). Preliminary seismic damage assessment of Mexican churches after September 2017 earthquakes, *Int. J. Arch. Herit.* **15,** no. 4, 505–525, doi: 10.1080/15583058.2019.1628323

Godínez-Domínguez, E. A., A. Tena-Colunga, L. E. Pérez-Rocha, H. I. Archundia-Aranda, A. Gómez-Bernal, R. P. Ruiz-Torres, and J. L. Escamilla-Cruz (2021). The September 7, 2017 Tehuantepec, Mexico, earthquake: Damage assessment in masonry structures for housing, *Int. J. Disaster Risk Reduct.* **56,** 102,123, doi: 10.1016/j.ijdrr.2021.102123.

Guo, R., Y. Zheng, J. Xu, and Z. Jiang (2019). Seismic and aseismic fault slip associated with the 2017 Mw 8.2 Chiapas, Mexico, earthquake sequence, *Seismol. Res. Lett.* **90,** no. 3, 1111–1120, doi: 10.1785/0220180262.

Hellel, M., J. L. Chatelain, B. Guillier, D. Machane, R. B. Salem, E. H. Oubaiche, and H. Haddoum (2010). Heavier damage without site effects and site effects with lighter damage: Boumerdes City (Algeria) after the May 2003 earthquake, *Seismol. Res. Lett.* **81,** no. 1, 37–43.

INEGI (2020). Mapas Geológicos, *Instituto Nacional de Estadística y Geografía*, available at https://www.inegi.org.mx/temas/geologia/default.html (last accessed September 2022) (in Spanish).

Kim, D., and K. Keranen (2018). Aftershocks of the 2016 Pawnee earthquake recorded by a dense nodal array, *Presented at 2018 AGU*, San Francisco, California (Fall Meet. Suppl.), Abstract.

Kim, Y., R. W. Clayton, and F. Keppie (2011). Evidence of a collision between the Yucatán block and Mexico in the Miocene, *J. Geophys. Int.* **187,** no. 2, 989–1000.

Konno, K., and T. Ohmachi (1998). Ground-motion characteristics estimated from spectral ratio between horizontal and vertical components of microtremor, *Bull. Seismol. Soc. Am.* **88,** no. 1, 228–241, doi: 10.1785/bssa0880010228.

Kreemer, C., G. Blewitt, and E. C. Klein (2014). A geodetic plate motion and Global strain rate model, *Geochem. Geophys. Geosys.* **15,** no. 10, 3849–3889, doi: 10.1002/2014GC005407.

Lane, J. W., E. A. White, G. V. Steele, J. C. Cannia, and J. H. Williams (2008). *Estimation of Bedrock Depth Using the Horizontal-to-Vertical (H/V) Ambient-Noise Seismic Method*, European Association of Geoscientists and Engineers, doi: 10.3997/2214-4609.20146351.

Laurendeau, A., P.-Y. Bard, F. Hollender, V. Perron, L. Foundotos, O.-J. Ktenidou, and B. Hernandez (2018). Derivation of consistent hard rock (1000 < VS < 3000 m/s) GMPEs from surface and down-hole recordings: Analysis of KiK-net data, *Bull. Earthq. Eng.* **16,** no. 6, 2253–2284, doi: 10.1007/s10518-017-0142-6.

Lay, T., L. Ye, H. Kanamori, Y. Yamazaki, K. F. Cheung, and C. J. Ammon (2013). The February 6, 2013 Mw 8.0 Santa Cruz Islands earthquake and tsunami, *Tectonophysics* **608,** 1109–1121, doi: 10.1016/j.tecto.2013.07.001.

Lermo, J., and F. J. Chávez-García (1994). Site effect evaluation at Mexico City: Dominant period and relative amplification from strong motion and microtremor records, *Soil Dynam. Earthq. Eng.* **13,** no. 6, 413–423, doi: 10.1016/0267-7261(94)90012-4.

Lynnes, C. S., and T. Lay (1988). Source process of the great 1977 Sumba earthquake, *J. Geophys. Res.* **93,** no. B11, 13407–13420, doi: 10.1029/JB093iB11p13407.

Melgar, D., and X. Pérez-Campos (2011). Imaging the Moho and subducted oceanic crust at the Isthmus of Tehuantepec, Mexico, from receiver functions, *Pure Appl. Geophys.* **168,** nos. 8/9, 1449–1460.

Melgar, D., X. Pérez-Campos, L. Ramirez-Guzman, Z. Spica, V. H. Espíndola, W. C. Hammond, and E. Cabral-Cano (2018). Bend faulting at the edge of a flat slab: The 2017 M_w 7.1 Puebla-Morelos, Mexico, earthquake, *Geophys. Res. Lett.* **45,** no. 6, 2633–2641, doi: 10.1002/2017GL076895.

Melgar, D., A. Ruiz-Angulo, E. S. Garcia, M. Manea, V. Xu, X. Ramirez-Herrera, M. T. Zavala-Hidalgo, J. Geng, J. Corona, N. Pérez-Campos, *et al.* (2018). Deep embrittlement and complete rupture of the lithosphere during the Mw 8.2 Tehuantepec earthquake, *Nature Geosci.* **11,** no. 12, 955–960, doi: 10.1038/s41561-018-0229-y.

Meng, L., H. Huang, Y. Xie, H. Bao, and L. A. Dominguez (2019). Nucleation and kinematic rupture of the 2017 Mw 8.2 Tehuantepec earthquake, *Geophys. Res. Lett.* **46,** no. 7, 3745–3754, doi: 10.1029/2018GL081074.

Nakamura, Y. (1989). A method for dynamic characteristics estimation of subsurface using microtremor on the ground surface, *Q. Rep. RTRI (Railw. Tech. Res. Inst.) (Jpn.)* **30,** no. 1, 25–30.

Nogoshi, M., and T. Igarashi (1971). On the amplitude characteristics of Microtremor (part 2), *Zisin (J. Seismol. Soc. Jpn. 2nd Ser.)* **24,** no. 1, 26–40, doi: 10.4294/zisin1948.24.1_26.

Ortega, R., D. Carciumaru, L. Quintanar, E. Huesca-Pérez, and E. Gutiérrez-Reyes (2019). A study of ground motion excitation based on the earthquake of September 8, 2017: Evidence that normal faults influence the stress parameter, *Pure Appl. Geophys.* **176,** no. 4, 1359–1377, doi: 10.1007/s00024-019-02150-2.

Pacheco, D., E. D. Mercerat, F. Courboulex, L. F. Bonilla, A. Laurendeau, and A. Alvarado (2021). Profiling the Quito basin (Ecuador) using seismic ambient noise, *Geophys. J. Int.* **228,** no. 2, 1419–1437.

Panzera, F., G. Lombardo, S. Imposa, S. Grassi, S. Gresta, S. Catalano, G. Romagnoli, G. Tortorici, F. Patti, *et al.* (2018). Correlation between earthquake damage and seismic site effects: the study case of Lentini and Carlentini, Italy, *Eng. Geol.* **240,** 149–162.

Pardo, M., and G. Suárez (1995). Shape of the subducted Rivera and Cocos plates in southern Mexico: Seismic and tectonic implications. *J. Geophys. Res.* **100,** no. B7, 12,357–12,373, doi: 10.1029/95JB00919.

Pérez-Campos, X., Y. H. Kim, A. Husker, P. M. Davis, R. W. Clayton, A. Iglesias, J. F. Pacheco, S. K. Singh, V. C. Manea, and M. Gurnis (2008). Horizontal subduction and truncation of the Cocos Plate beneath Central Mexico, *Geophys. Res. Lett.* **35,** no. 18, doi: 10.1029/2008gl035127.

Pozos-Estrada, A., M. M. Chávez, M. Á. Jaimes, O. Arnau, and H. Guerrero (2019). Damages observed in locations of Oaxaca due to the Tehuantepec Mw8.2 earthquake, Mexico, *Nat. Hazards* **97,** no. 2, 623–641, doi: 10.1007/s11069-019-03662-9.

Ringler, A. T., R. E. Anthony, M. S. Karplus, A. A. Holland, and D. C. Wilson (2018). Laboratory tests of Three Z-Land Fairfield Nodal 5-Hz, three-component sensors, *Seismol. Res. Lett.* **89,** no. 5, 1601–1608, doi: 10.1785/0220170236.

Sahakian, V. J., D. Melgar, L. Quintanar, L. Ramírez-Guzmán, X. Pérez-Campos, and A. Baltay (2018). Ground motions from the 7 and 19 September 2017 Tehuantepec and Puebla-Morelos, Mexico, earthquakes, *Bull. Seismol. Soc. Am.* doi: 10.1785/0120180108.

Schultz, C. A., S. C. Myers, J. Hipp, and C. J. Young (1998). Nonstationary Bayesian Kriging: A predictive technique to generate spatial corrections for seismic detection, location, and identification, *Bull. Seismol. Soc. Am.* **88,** 1275–1288.

Sedesol, BC Consultores Ambientales y de Riesgos S.C. (2012). Atlas de Riesgos Naturales del Municipio de Heroica Ciudad de Juchitán de Zaragoza, available at https://es.scribd.com/document/423564674/Atlas-Riesgos-Naturales-Juchitan-Oaxaca (last accessed April 2022).

Servicio Sismológico Nacional (SSN) (2018). Catálogo de Sismos, available at http://www2.ssn.unam.mx:8080/catalogo/ (last accessed December 2020).

Singh, S. K., M. Ordaz, L. Alcántara, N. Shapiro, V. Kostoglodov, J. F. Pacheco, S. Alcocer, C. Gutiérrez, R. Quaas, T. Mikumo, *et al.* (2000). The Oaxaca earthquake of 30 September 1999 (Mw = 7.5): A normal-faulting event in the subducted Cocos plate, *Seismol. Res. Lett.* **71,** no. 1, 67–78, doi: 10.1785/gssrl.71.1.67.

Singh, S. K., X. Pérez-Campos, V. H. Espíndola, V. M. Cruz-Atienza, and A. Iglesias (2014). Intraslab earthquake of 16 June 2013 (Mw 5.9), one of the closest such events to Mexico City, *Seismol. Res. Lett.* **85,** no. 2, 268–277, doi: 10.1785/0220130179.

Singh, S. K., G. Suárez, and T. Domínguez (1985). The Oaxaca, Mexico, earthquake of 1931: Lithospheric normal faulting in the subducted Cocos plate, *Nature* **317,** no. 6032, 56–58, doi: 10.1038/317056a0.

Site EffectS Assessment using AMbient Excitations (SESAME) European research project WP12-Deliverable D23.12 (2004). Guidelines for the implementation of the H/V spectral ratio technique on ambient vibration: Measurements, processing, and interpretations, available at http://sesame.geopsy.org/Delivrables/Del-D23-HV_User_Guidelines.pdf (last accessed September 2022).

Suárez, G. (2020). Large earthquakes in the Tehuantepec subduction zone: Evidence of a locked plate interface and large-scale deformation of the slab, *J. Seismol.* doi: 10.1007/s10950-020-09969-6.

Suárez, G., and P. Albini (2009). Evidence for great tsunamigenic earthquakes (M 8.6) along the Mexican subduction zone, *Bull. Seismol. Soc. Am.* **99,** no. 2A, 892–896.

Suárez, G., D. Ruiz-Barón, C. Chico-Hernández, and F. Ramón Zúñiga (2020). Catalog of preinstrumental earthquakes in central Mexico: Epicentral and magnitude estimations based on macroseismic data, *Bull. Seismol. Soc. Am.* **110,** no. 6, 3021–3036, doi: 10.1785/0120200127.

Suárez, G., M. A. Santoyo, A. Iglesias, V. Hjorleifsdottir, C. Villafuerte, and V. M. Cruz-Atienza (2019). Large scale lithospheric detachment of the downgoing Cocos plate: The 8 September 2017 earthquake (Mw 8.2), *Earth Planet. Sci. Lett.* **509,** 9–14, doi: 10.1016/j.epsl.2018.12.018.

Velasco, A. A., X. Pérez-Campos, A. Husker, M. S. Karplus, H. Gonzalez-Huizar, and S. A. Cortez (2020). La Crucecita earthquake illustrates quake risk in México, *Temblor* doi: 10.32858/temblor.097.

Wathelet, M., J.-L. Chatelain, C. Cornou, G. D. Giulio, B. Guillier, M. Ohrnberger, and A. Savvaidis (2020). Geopsy: A user-friendly open-source tool set for ambient vibration processing, *Seismol. Res. Lett.* **91,** no. 3, 1878–1889, doi: 10.1785/0220190360.

Wessel, P., and W. H. Smith (1998). New, improved version of Generic Mapping Tools released, *Eos* **79,** no. 47, 579.

Ye, L., T. Lay, Y. Bai, K. F. Cheung, and H. Kanamori (2017). The 2017 Mw 8.2 Chiapas, Mexico, earthquake: Energetic slab detachment, *Geophys. Res. Lett.* **44,** no. 23, 11,824–11,832, doi: 10.1002/2017GL076085.

Zhang, H., and M. R. Brudzinski (2019). Evidence for Rupture through a double Benioff zone during the 2017 Mw 8.2 Chiapas, Mexico earthquake, *Geophys. Res. Lett.* **46,** no. 2, 652–660, doi: 10.1029/2018GL080009.

Manuscript received 20 May 2021
Published online 23 December 2022